

## Shape memory alloy film damping for smart miniature systems

Shahabeddin Ahmadi, Kiran Jacob, Frank Wendler & Manfred Kohl

To cite this article: Shahabeddin Ahmadi, Kiran Jacob, Frank Wendler & Manfred Kohl (2018) Shape memory alloy film damping for smart miniature systems, International Journal of Smart and Nano Materials, 9:3, 199-215, DOI: [10.1080/19475411.2018.1496953](https://doi.org/10.1080/19475411.2018.1496953)

To link to this article: <https://doi.org/10.1080/19475411.2018.1496953>



© 2018 The Author(s). Published by Informa UK Limited, trading as Taylor & Francis Group.



Published online: 25 Jul 2018.



Submit your article to this journal [↗](#)



Article views: 96



View Crossmark data [↗](#)



# Shape memory alloy film damping for smart miniature systems

Shahabeddin Ahmadi<sup>a,b</sup>, Kiran Jacob<sup>a</sup>, Frank Wendler<sup>b</sup> and Manfred Kohl<sup>a</sup>

<sup>a</sup>Karlsruhe Institute of Technology (KIT), Institute of Microstructure Technology (IMT), Karlsruhe, Germany;

<sup>b</sup>Friedrich-Alexander University of Erlangen-Nürnberg (FAU), Dep. of Materials Science, Fürth, Germany

## ABSTRACT

This paper presents a dynamic analysis of the free and forced vibration of a free-standing bridge of superelastic shape memory alloy TiNiCuCo film with ultra-low fatigue properties and evaluates its versatility for novel miniature scale damping applications. A thermodynamics-based finite element model is used to simulate the evolution of martensite phase fraction during load-induced martensitic phase transformation. The effects of pre-strain, strain rate and excitation load on the hysteresis of stress-strain characteristics are investigated in order to assess damping energies. The analysis is performed under non-isothermal conditions taking into account heat transfer and rate-dependence of release and absorption of latent heat. We show that damping energy can be maximized by applying an optimum pre-strain. A maximum damping capacity of 0.17 is determined for the case of complete stress-strain hysteresis loop during phase transformation.

## ARTICLE HISTORY

Received 29 March 2018

Accepted 2 July 2018

## KEYWORDS

Shape memory alloy film; superelasticity; coupled finite element simulation; damping

## 1. Introduction

Damping and shock absorbing have gained increasing importance in engineering of novel lightweight technical structures as well as smart miniature systems. The global trend of miniaturization and increase of functionality enables the development of novel miniature electro-mechanical and opto-mechanical devices in a wide range of applications such as information technology, biomedical, automotive and aerospace [1,2]. Examples are, for instance, novel handheld systems carrying opto-mechanical, fluidic and sensible electronic components (e.g. for point-of-care diagnostics) as well as portable optical devices (cameras, smartphones), which are sensitive to motion and vibrations caused, e.g., by human activity. Other examples are autonomously operating systems [3], unmanned vehicles [4] or picosatellites [5]. Due to the close neighborhood of various functional units, these systems contain various sources of unwanted vibrations and loads that may disturb or even hinder the overall performance and, hence, need to be controlled.

SMA showing either the superelastic effect (SE) or shape memory effect (SME) are highly promising for damping applications [6,7]. SMA materials exhibit nonlinear stress-strain response and hysteresis due to a first order phase transformation allowing the engineering

**CONTACT** M. Kohl  [manfred.kohl@kit.edu](mailto:manfred.kohl@kit.edu)  Karlsruhe Institute of Technology (KIT), Institute of Microstructure Technology (IMT), Karlsruhe, Germany

© 2018 The Author(s). Published by Informa UK Limited, trading as Taylor & Francis Group.

This is an Open Access article distributed under the terms of the Creative Commons Attribution License (<http://creativecommons.org/licenses/by/4.0/>), which permits unrestricted use, distribution, and reproduction in any medium, provided the original work is properly cited.

and control of dissipative processes at large stress and strain levels up to 500 MPa and 5%, respectively. Owing to the underlying phase transformation, SE and SME are noise- and jerk-free. Due to a strong coupling of thermal, mechanical and electrical properties, SMA components exhibit multifunctional properties while keeping designs simple, which is of particular interest on small scales [8]. In the realm of miniature systems, SMA film base materials are in the focus of interest showing rapid heat transfer due to a large surface-to-volume ratio.

Damping applications usually demand for SMA materials showing sufficiently large dissipation of mechanical energy but low fatigue due to a highly reversible phase transformation. This leads to conflicting requirements as large dissipation involves a sufficiently large hysteresis, the hysteresis width being a measure of dissipated energy. However, low fatigue demands materials with low hysteresis showing high crystallographic compatibility between parent and product phase [9]. Here, a thermodynamics-based Gibbs free energy model is used to describe the nonlinear hysteretic performance of superelastic SMA material [10]. The model has been extended by a martensite-austenite interface free energy term using formulations from a phase-field model in order to describe the correlated mechanical and thermal local response of superelastic SMA films on a macro and mesoscopic ( $\mu\text{m}$ ) length scale, the formation and evolution of local strain and temperature bands, their tilt angle as well as strain-rate dependence [11].

Another challenge is the engineering of optimum geometries and adjustment of operation parameters to allow for maximum damping capacity. In the following, we investigate the damping performance of a miniature free-standing superelastic SMA bridge that is loaded by a rigid mass at its center. Base material is a SMA film of Ti-rich TiNiCuCo that has been shown to exhibit ultra-low fatigue behavior and, therefore, withstand a large number of load cycles [12]. However, the high crystallographic compatibility in the film results in a reduced hysteresis of superelastic plateau stress of about 100–150 MPa [13], which may adversely affect dissipation. In view of these conflicting material properties, the important question arises, how the new SMA materials could be useful for damping applications. In order to address this question, the nonlinear vibration characteristics and hysteresis-induced damping energy will be explored for the cases of free and forced vibration under non-isothermal conditions.

## 2. Simulation model

This section gives an overview of the damping setup and dynamic simulation model. As sketched in [Figure 1](#), a free-standing superelastic SMA bridge is used for damping of the deflection of rigid mass  $m$  in out-of-plane ( $z$ -) direction. The SMA bridge acts both as elastic

spring and damper element. Due to symmetry, only half of the setup is shown. In initial stress-free condition, the SMA bridge is in planar state. The proof mass  $m$  is applied at the center of the SMA bridge causing an initial deflection in negative  $z$ -direction. Pre-straining is accomplished by increasing the original length  $L_0$  of the SMA bridge as part of a preconditioning stage at the beginning of the simulation to  $L_0(1 + \varepsilon_{pre})$ . After reaching stationary conditions, an external force  $F(t)$  is applied to the

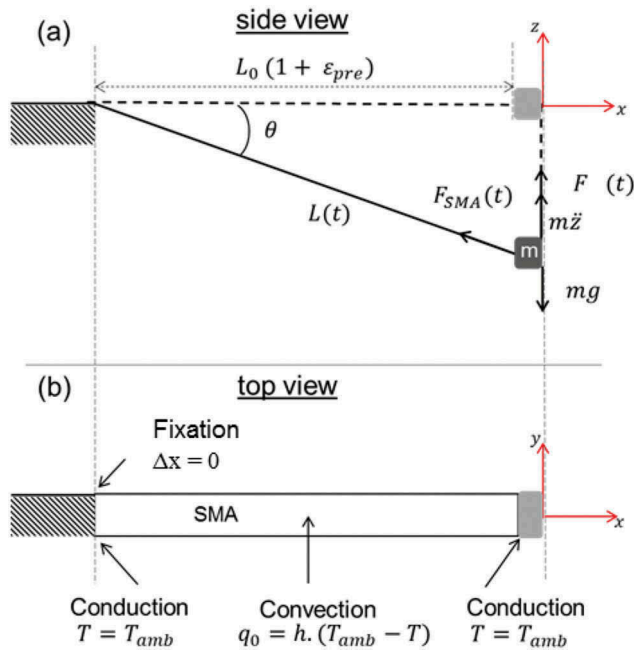


**Figure 1.** (a) Schematic of the damping setup. The force balance acting on the proof mass  $m$  comprises the gravitational force  $mg$ , inertia force  $m\ddot{z}$ , time-dependent external force  $F(t)$  and the dynamic response of the SMA bridge along tensile direction  $F_{SMA}(t)$ . (b) Schematic of simulation model including mechanical and thermal boundary conditions.

mass along  $z$ -direction, which is either a short step-like loading pulse causing free vibration of the mass or a continuous forced harmonic loading signal. As a result, the SMA bridge is loaded by the force  $F_{SMA}(t)$  along its tensile direction. The effects of load and load rate (load frequency) on the dissipated energy are investigated for given dimensions of SMA bridge and mass.

### 2.1. SMA material model

A number of theoretical models have been developed in order to describe the super-elastic behavior of SMA materials, for a recent review see, for example, Refs. [14,15]. Here, the mechanical response of the SMA bridge is described in a thermodynamic approach using an extended Müller-Achenbach-Seelecke (MAS) model [10,16], which takes energy contributions from martensite-austenite interfaces into account as detailed in [11]. The model does neither consider structural anisotropy nor texture. For the correct treatment of thermomechanical response including local strain effects, a mesoscopic resolution of the material domain has shown to be necessary. In the following, we briefly summarize the governing equations for martensite kinetics, mechanical displacement and temperature evolution.

In the thermodynamic model, transitions between tension adapted martensite  $M_+$ , compression adapted martensite  $M_-$  and austenite  $A$  are considered. Possible transition paths are determined by the Gibbs free energy density  $g(\sigma, \varepsilon, T) = \Psi(\varepsilon, T) - \sigma\varepsilon$  being a

scalar function of strain  $\varepsilon$ . The elastic energy density  $\Psi(\varepsilon, T)$ , which is constructed from piecewise parabolic functions, defines the equilibrium states of  $M_+$ ,  $M_-$  and  $A$  under stress-free conditions. The martensitic transition is described within the framework of transition state theory as a thermally activated process across the energy barriers defined by  $\Psi(\varepsilon, T)$ , that separate the equilibrium states. Motivated by phase-field modelling, austenite-martensite interface energy terms are included, which are quantified by the parameters  $\tilde{\gamma}$  and  $\delta$  denoting interfacial free energy and width of the austenite-martensite transition, respectively. The rate equations for the local phase fractions  $x_\alpha$  ( $\alpha \in \{M_+, M_-, A\}$ ) then write [11]:

$$\dot{x}_{M_+} = -x_{M_+}p^{M_+A} + x_Ap^{AM_+} + \tilde{\gamma}\nabla^2x_{M_+} - 9\frac{\tilde{\gamma}}{\delta^2}x_{M_+}(1-x_M)(1-2x_M) \quad (1)$$

$$\dot{x}_{M_-} = -x_{M_-}p^{M_-A} + x_Ap^{AM_-} + \tilde{\gamma}\nabla^2x_{M_-} - 9\frac{\tilde{\gamma}}{\delta^2}x_{M_-}(1-x_M)(1-2x_M) \quad (2)$$

$$\dot{x}_A = -\dot{x}_{M_+} - \dot{x}_{M_-} \quad (3)$$

In Eqs. (1,2), the martensite phase fraction is given by  $x_M = x_{M_+} + x_{M_-}$ . In the view of the phase-field model,  $x_M$  is a single order parameter that discerns between the thermodynamic phases  $A$  and  $M_+, M_-$ , so we neglect interfacial energy between the variants  $M_+$  and  $M_-$ . Equation (3) follows from the summation condition  $x_{M_+} + x_{M_-} + x_A = 1$ . The transition rate coefficients  $p^{\alpha\beta} = p^{\alpha\beta}(\sigma^{\alpha\beta} - \sigma, T)$  with  $(\alpha, \beta \in \{M_+, M_-, A\})$  are derived in closed form as nonlinear functions of temperature and stress, which represent the driving forces for transition. A linear temperature dependency of the plateau stresses for an  $\alpha \rightarrow \beta$  transition is defined by the Clausius-Clapeyron coefficients  $C^{\alpha\beta}$ ,

$$\sigma^{\alpha\beta}(T, r) = \left[ \sigma_0^{\alpha\beta} + C^{\alpha\beta}(T - T_{ref}) \right] \cdot (1 + \xi(r)). \quad (4)$$

In Equation (4),  $\xi(r)$  is a local log-normal distributed random noise that has to be adapted specifically for the polycrystalline material of the sample. It accounts for material heterogeneity and enables nucleation of local transformation bands [11].

The mechanical evolution of the SMA domain is captured by the elastodynamic equation

$$\rho\ddot{u} = -\nabla \cdot \sigma, \quad (5)$$

where the small strain approximation under plane stress conditions is applied to calculate the strain tensor  $\varepsilon_{ij} = \frac{1}{2}(\partial u_i/\partial x_j + \partial u_j/\partial x_i)$  from the displacement field  $u$ . Isotropic Hooke's law is used as the constitutive relationship,  $\sigma = C(x)(\varepsilon - \varepsilon_T(x))$ , where  $\varepsilon_T(x)$  denotes the transformation strain tensor, describing relative deformations of  $M_+$  and  $M_-$  with respect to the parent phase  $A$ . Both elastic tensor  $C(x)$  and  $\varepsilon_T(x)$  are local averages using the phase fractions  $x = (x_{M_+}, x_{M_-}, x_A)^T$  [11]. Extra Rayleigh or viscous terms in Equation (5) are not included at this stage of the study, as we consider the hysteretic damping during martensitic transformation as the major effect.

**Table 1.** Simulation parameters are taken from own experimental work [17,18]. Thermal conductivities of austenite and martensite are taken from [19].

Parameter	Symbol	Value
proof mass	$m$	0.01 kg
Length of SMA bridge	$l$	0.01 m
Width of SMA bridge	$w$	0.00035 m
Thickness of SMA bridge	$d$	$20 \times 10^{-6}$ m
Critical stress for A – M transformation	$\sigma_{AM}$	242 MPa
Critical stress for M – A reverse transformation	$\sigma_{MA}$	134 MPa
Reference temperature	$T_{ref}$	294 K
Clausius–Clapeyron coefficient (A – M transf.)	$C^{AM}$	10.4 MPa/K
Clausius–Clapeyron coefficient (reverse transf.)	$C^{MA}$	14 MPa/K
Transformation strain	$\epsilon_T$	0.0075
Elastic modulus of austenite	$E(A)$	$35.9 \times 10^9$ Pa
Elastic modulus of martensite	$E(M)$	$16.0 \times 10^9$ Pa
Latent heat	$L$	5600 J/kg
Thermal conductivity of austenite	$\kappa(A)$	18 W/m/K
Thermal conductivity of martensite	$\kappa(M)$	8.6 W/m/K
Ambient temperature	$T_{ambient}$	294 K
Heat transfer coefficient	$h$	30 W/m <sup>2</sup> /K

Finally, for heat transport and generation due to the first order transformation we apply the balance equation

$$\rho c_p \dot{T} = \nabla \cdot k(x) \nabla T + \Delta h^{AM}(\sigma, x) \quad (6)$$

with  $k(x)$  being the locally averaged heat conductivity and  $\Delta h^{AM}(\sigma, x)$  the stress-dependent transformation enthalpy. The latter includes all caloric effects from the A–M and M–A transitions, and is in first order identical to the entropy-change related latent heat  $L$ . The simulation parameters are summarized in Table 1.

## 2.2. Dynamic model of SMA bridge

The damping performance of the system given by the proof mass  $m$  attached to the SMA bridge is determined by the dynamic evolution of stress and strain of SMA material. Due to the small thickness of the SMA material we neglect elastic contributions from bending, which would arise at the supporting frame and proof mass, where the film is fixed (Figure 1(a)). Hence, we can describe the 3D out-of-plane oscillation of the bridge structure by plane-stress simulation of the tensile loaded SMA material. Due to symmetry, an identical force from a second SMA bridge is considered. The equation of motion for the proof mass in z-direction is given by the force balance (Figure 1(a)):

$$m\dot{v} - mg + 2F_{SMA}(t)\sin(\theta) - F(t) = 0 \quad \sin(\theta) = \frac{z(t)}{\sqrt{z(t)^2 + l_0^2(1 + \epsilon_{pre})^2}}, \quad (7)$$

with the velocity  $v = \dot{z}$ , the external force  $F(t)$  and dynamic response of the SMA bridge along tensile direction  $F_{SMA}(t)$ . The geometric transformation between in- and out-of-plane motion strongly reduces the computational costs.

In the SMA domain, discretized by a fine triangular mesh, the differential equations for the displacement and temperature evolution are solved using the solid mechanics and heat transport modules of the finite element software COMSOL Multiphysics. User

defined functions for the elastic modulus, transformation strain and the heat source terms are used. For the kinetic equations Equations (1–3), a general PDE solver module is customized and the local maximum shear stress (Tresca stress) is applied to calculate the transition rates.

Using the force  $F_{SMA}(t)$  as an output of the FEM simulation, the motion of mass Equation (7) is numerically solved after each time step with an COMSOL ODE module (initial condition  $z(0) = 0$ ,  $\dot{z}(0) = 0$ ). The resulting velocity  $v \sin(\theta)$  in the plane of SMA bridge is applied as a boundary condition to the right side of the SMA domain, whereas at its left boundary, the displacements are set to zero (rigid support). After each time step, the force at the right boundary of the SMA domain is evaluated by averaging and used as a new input force  $F_{SMA}(t)$  for the next solution step of the ODE. All other boundaries are set to be stress-free.

Constant ambient temperature boundary conditions  $T = T_{amb}$  are applied to the ends of the SMA bridge, assuming an unchanged temperature of the connected supporting structure and mass during the duration of the simulation. For all other temperature boundaries we extract heat according to Newton's law of cooling with a flux of  $q_0 = h(T_{amb} - T)$ , in which  $h$  is a heat transfer coefficient. All boundary conditions are depicted in Figure 1(b).

To capture the transient processes during vibration, a maximum solution time step width of  $10^{-3}$  s and a time step for data storage of  $2 \times 10^{-4}$  s are chosen. This leads to approximately  $10^4$  time frames spanning the duration of several seconds of operation time. By switching off the dissipative dynamics of the martensitic transformation, it was verified that the numerical solution was completely energy preserving during the simulation period.

### 3. Material properties

Currently, TiNiCu-based films receive considerable attention due to their ultra-low fatigue properties [12], which is of special interest for various applications with high demands on fatigue lifetime including damping applications. However, the corresponding phase transformation in these films exhibits a rather narrow hysteresis. Therefore, it is important to investigate how the material properties of TiNiCuCo films affect energy dissipation and how the performance of corresponding damper systems could be optimized.

The material properties of free-standing pseudoelastic TiNiCuCo films are taken from our recent experimental work [18,19]. Typical engineering stress-strain characteristics of a TiNiCuCo film are plotted in Figure 2 for the strain rates of  $10^{-3}$  and  $10^{-2} \text{ s}^{-1}$  corresponding to isothermal and nearly adiabatic conditions, respectively. The numerical results reproduce the experimental characteristics at different strain rates. In particular, the critical stress for stress-induced onset of martensitic transformation is about 220 MPa, the corresponding critical strain is about 0.007. The increase in slope of the superelastic plateau during loading is due to austenite stabilization by self-heating at higher strain rates. On reaching the maximum strain during loading, the strain is held constant for a period of 10 s resulting in a steep stress reduction. The relaxation effect is higher at larger strain rates. The slope of pseudoelastic plateau upon unloading also

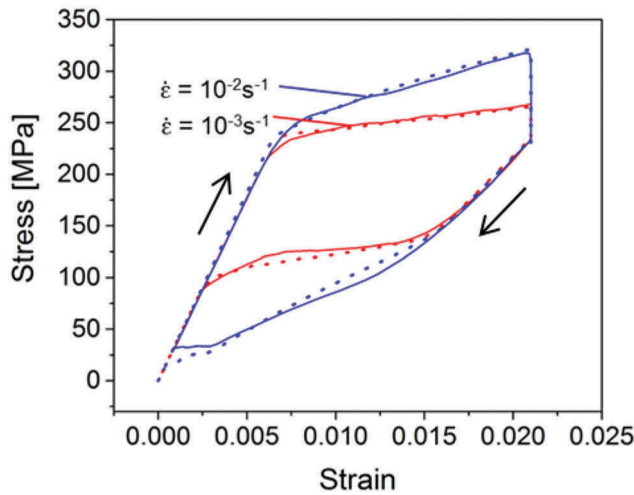


**Figure 2.** Simulated and experimental stress-strain characteristics of a TiNiCuCo sample at different strain rates as indicated. The continuous line represents experimental data and the dotted line simulation results. The simulation parameters are listed in Table 1.

depends on strain rate due to self-cooling [11]. The area enclosed by the loading and unloading curves represents the work per unit volume, which is dissipated in a cyclic operation. Higher dissipation is observed in the case of higher strain rate. The dissipation increases until the adiabatic condition is reached at a strain rate of about  $0.2 \text{ s}^{-1}$  [18].

## 4. Damping performance

### 4.1. Free vibration

The free vibration analysis is performed by applying a short step-like excitation load  $F_{exc}$  of 20 ms to the mass along z-direction. Before, the SMA bridge is loaded by the mass of 10 g causing an initial deflection of  $-0.7 \text{ mm}$ . Additional pre-straining is performed by linearly ramping up the length parameter  $L_0(t)$  in Equation (7) from  $L_0$  to  $(1 + \varepsilon_{pre})L_0$  within 0.25 s at the beginning of the simulation. Subsequently, the pre-strained device is allowed to reach stationary conditions during the time of 0.25–0.5 s. The time-dependent response of the mass and of the SMA bridge after 0.52 s is investigated for various values of pre-strain and excitation load.

Figure 3(a) shows the simulated evolution of amplitude and martensite phase fraction for an excitation load of 0.525 N corresponding to the critical stress for onset of martensitic phase transformation of 230 MPa. No additional pre-strain is applied in this case. The excitation load deflects the mass upwards in z-direction causing an initial strain release and subsequent strain increase after reaching positive values of deflection. As a consequence, a stress-induced phase transformation occurs resulting in an increase of martensite phase fraction  $x_{M_+}$ . The first maximum of phase fraction  $x_{M_+}$  correlates with the reversal point of positive deflection. Subsequent decrease of deflection results in a decrease of martensite phase fraction. Due to inertia force, the mass deflects further downwards below the stationary equilibrium position and reaches negative deflections causing the second

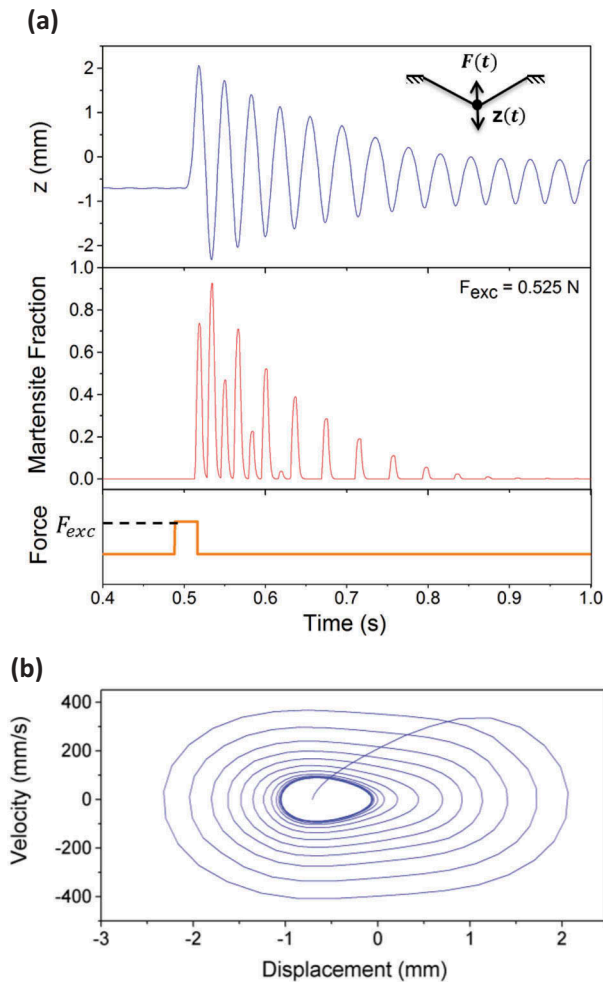


**Figure 3.** (a) Time-dependent vibration amplitude  $z$  of the mass and corresponding evolution of martensite phase fraction  $x_{M+}$  in the SMA bridge for an excitation load of 0.525 N. (b) Velocity-displacement characteristic during the investigated time period of 0.5–1 s.

stress-induced phase transformation. Thus, the second maximum of phase fraction  $x_{M+}$  occurs that correlates with the reversal point of negative deflection. The maximum phase fraction reaches almost 1 indicating almost complete phase transformation.

Overall, two phase transformation events occur within an oscillation cycle with the corresponding dissipation of kinetic to thermal energy. The larger peak of martensite fraction in the second half-cycle is attributed to the larger negative deflections caused by acceleration due to gravity. As viscous damping in air and intrinsic structural damping are neglected in the simulation, oscillation continues at low deflections at an eigenfrequency of 30 Hz when the elastic regime is reached.

The corresponding velocity-displacement characteristic is shown in Figure 3(b). Starting from the initial deflection of  $-0.7$  mm at zero velocity, the velocity performs oval trajectories, whose distance decreases due to damping. The asymmetry along the

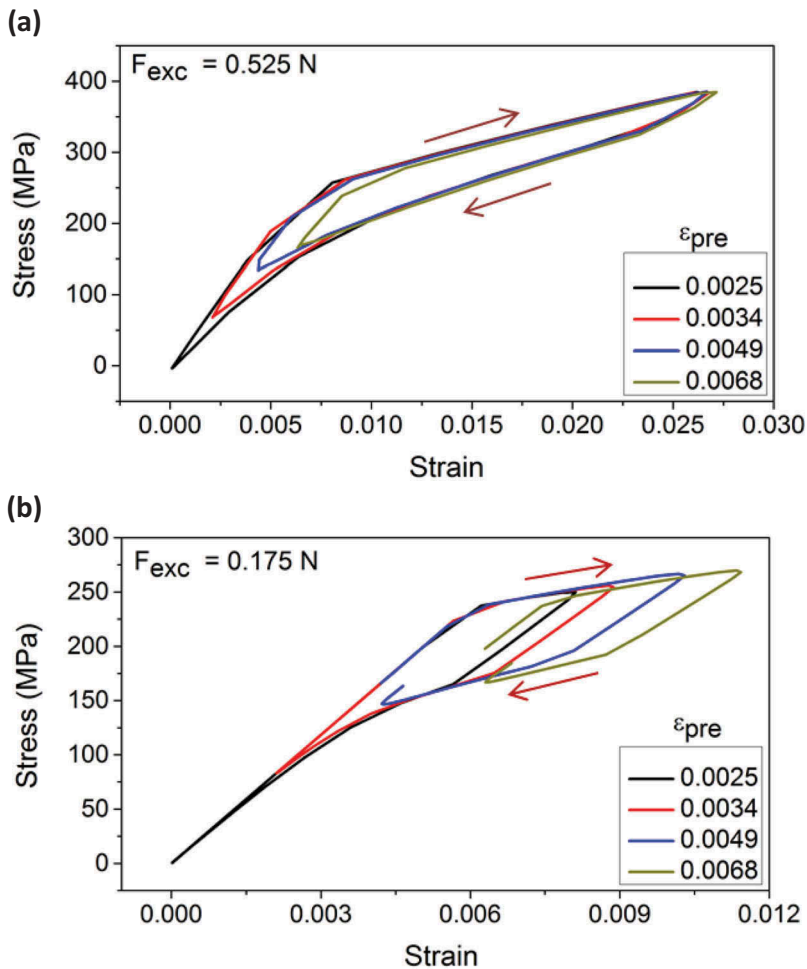


**Figure 4.** Stress-strain loops calculated for the SMA bridge during the first loading cycle for excitation loads of 0.525 (a) and 0.175 N (b). The different values of pre-strain are indicated.

displacement direction is a consequence of gravity. The changes in velocity reflect the strain rate of the SMA bridge during vibration. The maximum velocity is about 400 mm/s during the first cycle and decreases more strongly in the initial phase of oscillation. After about 10 oscillation cycles, the elastic regime at low deflections is reached, at which the characteristics become stationary.

Figure 4(a) and (b) show simulated stress-strain loops for excitation loads of 0.525 and 0.175 N, respectively, as well as various values of pre-strain. In each case, the second stress-induced phase transformation cycle (starting in negative  $z$ -direction), is considered.

As stated before, almost complete phase transformation occurs at the excitation load of 0.525 N and zero pre-strain. For increasing pre-strain up to 0.0068, the minimum strain of the stress-strain loops increases accordingly, while the maximum strain remains almost unchanged. As the end of the stress-strain plateau is reached in these cases, a larger increase of stress would be required to further increase the strain into the elastic

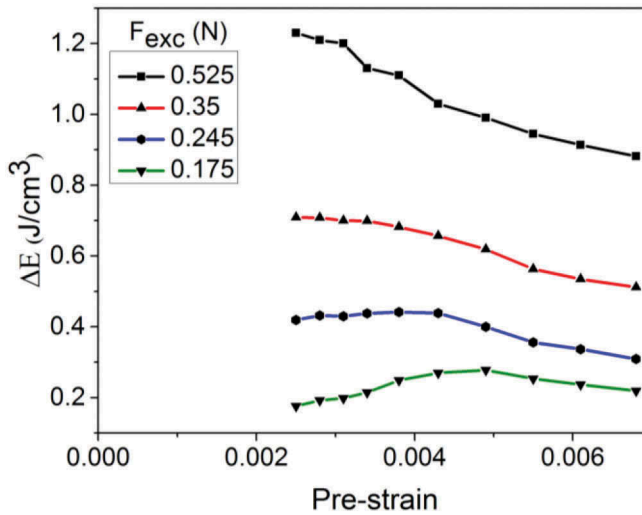


**Figure 5.** Calculated values of dissipation energy density as a function of pre-strain  $\epsilon_{pre}$  for different excitation loads  $F_{exc}$ .

regime of martensite. At the low excitation load of 0.175 N, both the minimum and maximum strain of the stress-strain loops increase and thereby shift into the superelastic region as shown in Figure 4(b). For pre-strain of 0.0049 and above, the mismatch of starting and ending points of the loops indicates the accumulation of martensite during load cycling.

The effects of the various loading conditions of pre-strain and excitation load on the energy dissipation are summarized in Figure 5. The dissipated energy density  $\Delta E = \frac{1}{V} \oint \sigma d\epsilon$  during the stress-strain cycle is calculated from the simulation data,  $V$  being the volume of SMA material. For an excitation load of 0.525 N, the average Tresca stress in the SMA material is determined to be about 230 MPa. The corresponding maximum dissipated energy density  $\Delta E$  is about 1.2 J/cm<sup>3</sup>. Taking into account the volume of SMA material and input of maximum deformation work  $W$  the corresponding damping capacity  $\Delta E/W$  is determined to be about 0.17. Note that the minimum pre-strain of 0.0025 is caused by the weight of the proof mass. In this case, the SMA material traverses the full stress-strain cycle despite the low pre-strain.

For increasing pre-strain, the dissipated energy density decreases as the SMA material traverses only a sub-loop of the full stress-strain cycle having a smaller enclosed area (see Figure 4(a)). For the smaller excitation load of 0.35 N, a similar trend is found. For increasing pre-strain, the SMA material traverses sub-loops of the full stress-strain cycle that shift to higher strain values. As a consequence, the area enclosed by the stress-strain loops gradually decreases. For low excitation loads, a different behavior is observed. In these cases, an optimum value of pre-strain exists, at which the energy dissipation becomes maximal. An initial increase of energy dissipation occurs for increasing pre-strain, which is attributed to the initial elastic deformation at small pre-strain, which does not contribute to energy dissipation unless the onset of stress-induced martensitic transformation is reached. For

decreasing excitation load from 0.245 to 0.175 N, the optimum pre-strain increases from about 0.0043 to 0.0049 corresponding to about 60 and 70% of critical strain for the onset of martensitic transformation, respectively.

#### 4.2. Forced vibration

In the forced vibration analysis, a harmonic excitation load  $F_{exc}\sin(2\pi ft)$  is applied to the mass along z-direction. In the following, we consider a maximum excitation load  $F_{exc}$  of 0.105 N. The pre-strain is chosen to be 0.0049 (70% of critical strain for the onset of martensitic transformation), which is near the optimum value. During a pre-conditioning phase of 0.25 s, both harmonic excitation load and pre-load are ramped up linearly to their maximum values. The time-dependent response of the mass and of the SMA bridge (martensite fraction and stress-strain response) are investigated as a function of frequency.

Figure 6 shows the simulated vibration amplitude and martensite phase fraction caused by the harmonic loading signal for a frequency of 32 Hz. An overview of the frequency dependence of vibration amplitudes is depicted in the inset of Figure 7 indicating that harmonic loading occurs close to resonance. Again, deflections in positive and negative z-direction are accompanied by stress-induced phase transformations and two maxima of martensite fraction  $x_{M_+}$  occur during a single oscillation cycle. The initial phase during the first second is characterized by a beating effect in vibration amplitude originating from the coupling of vibrations of SMA bridge in z- and y-direction. Our analysis of the vibration amplitudes of SMA bridge in z- and y-direction (not presented here) clearly shows that they are alternating in time with a ratio of about 200, which is in

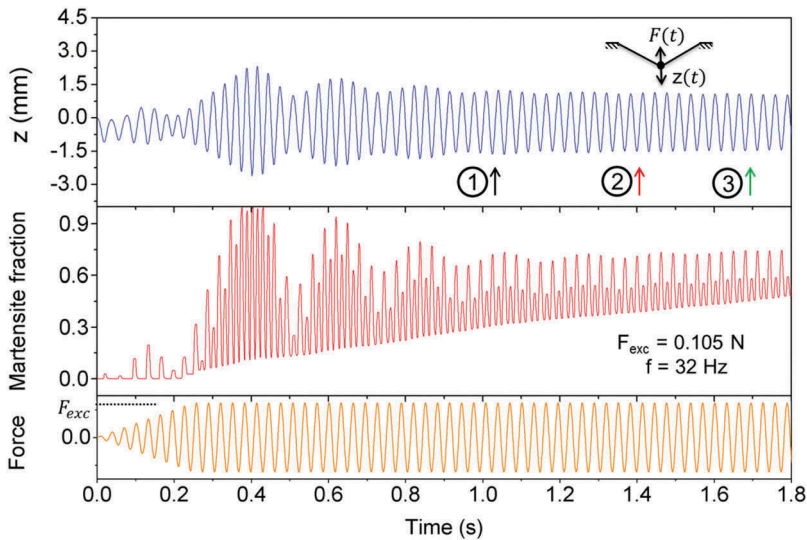
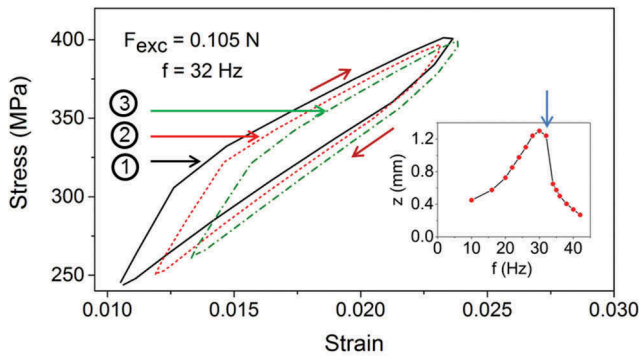


Figure 6. Simulation of vibration amplitude of the mass  $z$  and corresponding change of martensite phase fraction in the SMA bridge  $x_{M_+}$  during harmonic loading with force  $F(t)$  at 32 Hz and pre-strain  $\epsilon_{pre}$  of 0.0049. Vibration cycles highlighted by arrows correspond to the stress-strain loops shown in Figure 7.



**Figure 7.** Stress-strain loops corresponding to the vibration cycles indicated in Figure 6 (top panel) by arrows. The inset shows the frequency dependence of vibration amplitudes indicating that excitation occurs near resonance.

line with the stiffness ratio of the bridge in both directions. As this effect is not specific to damping based on superelastic SMA materials, it will be not considered any further in this investigation. Within about 1 s, beating abates and oscillation amplitude stabilizes. However, for increasing number of oscillations, the martensite fraction continuously increases for each cycle to higher values indicating martensite accumulation. This behavior is also observed in Figure 7 showing a drift of stress-strain loops corresponding to the oscillation cycles indicated in Figure 6 by arrows. As a consequence, the area enclosed by the stress-strain loops decreases for increasing number of oscillations and, thus, the damping capacity decreases as well.

Figure 8 shows simulated vibration amplitude and change of martensite phase fraction for the case of harmonic loading well below resonance at 16 Hz. In this case, the initial beating effect is much less pronounced and the vibration amplitude stabilizes

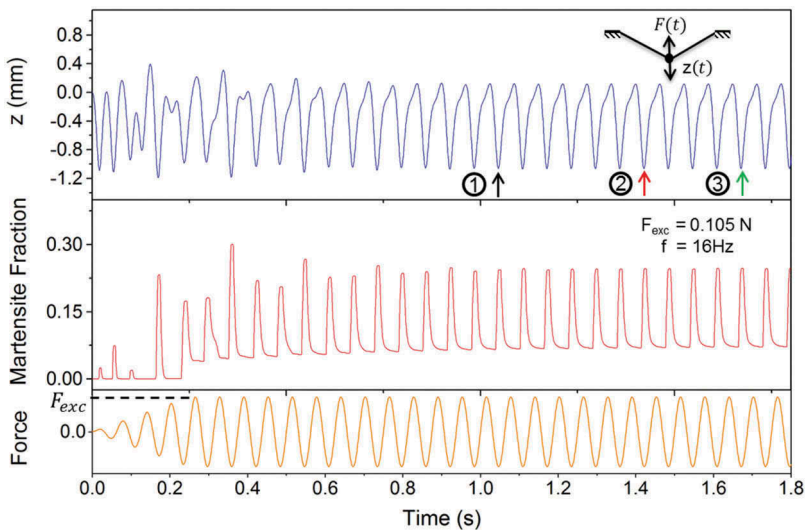


**Figure 8.** Simulation of vibration amplitude of the mass  $z$  and corresponding change of martensite phase fraction in the SMA bridge during harmonic loading with force  $F(t)$  at 16 Hz and pre-strain  $\epsilon_{pre}$  of 0.0049. Vibration cycles highlighted by arrows correspond to the stress-strain loops shown in Figure 9.

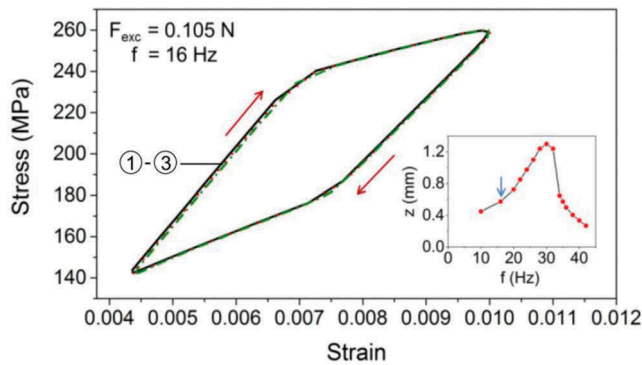


**Figure 9.** Stress-strain loops corresponding to the vibration cycles indicated in Figure 8 (top panel) by arrows. The inset shows the frequency dependence of oscillation amplitudes indicating that excitation occurs well below resonance.

earlier after about 0.7 s. In this case, martensite accumulation is insignificant. Accordingly, the stress-strain loops corresponding to different oscillation cycles closely overlap as shown in Figure 9. However, the maximum strain does not exceed 1% and, thus, much less energy can be dissipated compared to the resonance case.

## 5. Discussion

The damping performance of a TiNiCuCo bridge device is assessed by FE simulations based on a thermodynamics-based model. The SMA bridge is loaded in its center in out-of-plane direction, which allows inducing a martensitic phase transformation in tensile direction. The model allows simulating the effects of pre-strain and excitation load on the evolution of martensite phase fraction during phase transformation. Optimum damping performance is determined by seeking for maximum hysteresis of the stress-strain loop during load cycling. When the load cycle shifts to the elastic regimes of either austenite or fully transformed martensite state, dissipation decreases and consequently hysteretic damping is less effective. The model of SMA material behavior is validated by comparing simulation and experiment for tensile loading under isothermal and nearly adiabatic loading conditions corresponding to strain rates of  $10^{-3}$  and  $10^{-2} \text{ s}^{-1}$ , respectively.

Applying short loading pulses with low force only causes partial phase transformation and thus limits the damping of mass vibration. In this case, the material undergoes minor hysteresis loops, which depend on the detailed microstructure of the SMA material and material heterogeneity. Within the context of the FE model the statistical distribution of the critical transformation stresses affects the course minor stress-strain loops, a parameter which still has to be adapted. Therefore, the presented results on dissipation energy have to be considered as idealized values assuming a homogeneous critical stress in the whole SMA material that may underestimate the real performance in an inhomogeneous SMA material. We show that applying a pre-strain is useful to assist the excitation load in order to overcome the critical stress for onset of martensitic phase transformation. For low excitation forces, an optimum pre-strain exists to achieve maximum hysteresis and thus maximal dissipation, which is the anticipated mode of operation. Further increase of pre-strain causes

an increase of the maximum strain of stress-strain loop, but the minimum strain increases as well causing the overall hysteresis to decrease.

For increasing load, the required pre-strain decreases and eventually becomes zero at optimum excitation load. In this case, full phase transformation can be achieved and, thus, the full hysteresis can be exploited for damping without assistance by pre-strain. The maximum dissipated energy density is determined to be about  $1.2 \text{ J/cm}^3$ , corresponding to a maximum damping capacity of 0.17. For too high excitation load, stress values exceed the stress plateau region and reach the regime of fully transformed martensite. Therefore, hysteresis becomes small again resulting in limited damping performance. In addition, material degradation due to plastic deformation is likely to occur.

Harmonic loading is considered for low excitation loads at optimum pre-strain for the cases of non-resonant and resonant condition. In each case, an initial transient of vibration in z-direction in the form of a beating signal is observed, which also occurs less pronounced at other frequencies, while the beating frequency does not change (compare [Figures 6](#) and [8](#)). Comparing vibration amplitudes in z- and y-direction we refer this effect to the coupling of vibrations of SMA bridge in z- and y-direction. After about ten oscillations (0.7 s) stationary conditions occur, which are characterized by fully reversible phase transformation cycles. In the case of small load of 0.105 N presented here, energy dissipation is well below the maximum possible value. Therefore, load amplitude may be further increased up to a factor of about 5 until maximal possible energy dissipation is reached.

At resonance, full martensitic transformation occurs for the investigated load amplitude. In this case, maximum damping capacity is determined to be 0.17. However, stationary conditions are not reached in the investigated time window due to incomplete reverse transformation causing accumulation of martensite for increasing number of load cycles. The associated remnant strain causes a decrease of stress. As a consequence, a reduced fraction of martensite contributes to phase transformation and consequently, dissipation energy is expected to decrease until stationary conditions are reached. Our simulations show that this effect is a characteristic feature of super-elastic SMA damping at large excitation loads.

When increasing the frequency above resonance, high load rates lead to adiabatic conditions and significant self-heating. It has been shown for the SMA material in this investigation that these effects cause an increase of the slope of stress plateau and of hysteresis [[20](#)]. However, energy dissipation remains well below the case of resonant loading. Due to self-heating and cooling, an oscillatory behavior of temperature occurs following the frequency-dependent course of excitation load. Thereby, heat may accumulate causing an increase of overall temperature with time. This effect is particularly pronounced at resonance. As the frequency approaches resonance, we observe a maximum temperature change of about 5 K under stationary conditions after about 1 s (compare [Figure 6](#)). In addition, the minimum temperature rises by about 7.5 K from the initial reference temperature of 294 K due to heat accumulation. It is important to note that the presented results represent idealized material properties. In real SMA materials depending on the detailed microstructure, some fraction of martensite may not contribute to reversible cycling after reaching the end of stress plateau due to microstructure-dependent high critical stress values for onset of phase transformation [[21](#)].

## 6. Conclusions

SMA materials are of special interest for damping applications, as they exhibit significant energy dissipation during load cycling, which correlates with the hysteresis of the stress-strain loop during stress-induced martensitic phase transformation. SMA films are particularly promising for damping applications at miniature scales. Their thickness and lateral dimensions can be adjusted with large flexibility in order to match the material response to the excitation load. Many damping applications require SMA materials that withstand a large number of load cycles. Therefore, this research focuses on TiNiCuCo films, which have recently been shown to exhibit ultra-low fatigue.

A free-standing superelastic SMA bridge is used for damping of the deflection of a proof mass in out-of-plane direction. Investigations of free oscillation after applying a short step-like excitation load and of forced oscillation by harmonic loading show dissipation due to stress-induced phase transformation. For a given SMA bridge design, low excitation loads cause partial phase transformations. In this case, dissipation can be maximized by applying an optimum pre-strain. No pre-strain is needed at sufficiently large excitation load required to induce complete phase transformation. In this case, the maximum damping capacity of 0.17 is observed. During harmonic loading at resonance and out-of resonance at sufficiently high load, a reduction of damping capacity gradually occurs due to accumulation of martensite. Overall, the achieved results for TiNiCuCo materials are lower than maximum values reported on damper systems based on conventional SMA materials, which may reach damping capacity above 0.5 [22]. This reduced damping performance has to be considered as a tradeoff, as TiNiCuCo materials are optimized for long fatigue life.

So far, damping performance has been evaluated on the macroscale level taking into account the evolution of the overall martensite fraction and corresponding change of engineering stress and strain as a function of time. The simulation model has been experimentally validated for the investigated TiNiCuCo films by tensile experiments under isothermal and adiabatic conditions. As next steps, the reported time dependence of dissipation and maximum dissipation values need to be verified for TiNiCuCo bridge devices. Furthermore, the simulation model will be used to investigate the evolution of stress-induced phase transformation on the mesoscale with spatial resolution of a few tens of micrometer, which is accessible experimentally by digital image correlation and infrared thermography. This will allow for understanding the influence of strain band formation and evolution on the load-dependence of dissipation and fatigue.

## Acknowledgments

The authors gratefully acknowledge funding by the German Science Foundation (DPG) within the priority program SPP1897 'Calm, Smooth and Smart – Novel Approaches for Influencing Vibrations by Means of Deliberately Introduced Dissipation.

## Disclosure statement

No potential conflict of interest was reported by the authors.

## Funding

This work was supported by the German Science Foundation DFG [WE 4747/-];

## References

- [1] H. Zappe, *Fundamentals of Micro-Optics*, Cambridge: Cambridge University Press, 2010.
- [2] A. Lenk, R.G. Ballas, R. Werthschützky, and G. Pfeifer, *Electromechanical Systems in Microtechnology and Mechatronics*, Berlin: Springer, 2011.
- [3] I. Colomina and P. Molina, *Unmanned aerial systems for photogrammetry and remote sensing: A review*, ISPRS J. Photogrammetry Remote Sensing 92 (2014), pp. 79–97. doi:10.1016/j.isprsjprs.2014.02.013
- [4] J. Primicerio, S.F. Di Gennaro, E. Fiorillo, L. Genesio, E. Lugato, A. Matese, and F.P. Vaccari, *A flexible unmanned aerial vehicle for precision agriculture*, Precision Agric. 13 (2012), pp. 517–523. doi:10.1007/s11119-012-9257-6
- [5] N.F. De Rooij, S. Gautsch, D. Briand, C. Marxer, G. Mileti, W. Noell, H. Shea, U. Stauffer, and B. Van Der Schoot, MEMS for space, Proceedings of Transducers 2009, Denver, CO, USA, June 21–25(2009) 17–24.
- [6] E.J. Graesser and F.A. Cozarella, *Shape memory alloys as new materials for seismic isolation*, J. Eng. Mech. ASCE 117 (11) (1991), pp. 590–608. doi:10.1061/(ASCE)0733-9399(1991)117:11(2590)
- [7] V. Torra, C. Auguet, A. Isalgue, G. Carreras, P. Terriault, and F.C. Lovey, *Built in dampers for stayed cables in bridges via SMA. The SMARTeR-ESF project: A mesoscopic and macroscopic experimental analysis with numerical simulations*, Eng. Structures 49 (2013) (2013), pp. 43–57. doi:10.1016/j.engstruct.2012.11.011
- [8] M. Kohl, *Shape Memory Microactuators*, Springer, Heidelberg, 2004.
- [9] R. Zarnetta, R. Takahashi, M.L. Young, A. Savan, Y. Furuya, S. Thienhaus, B. Maass, M. Rahim, J. Frenzel, H. Brunken, Y.S. Chu, V. Srivastava, R.D. James, I. Takeuchi, G. Eggeler, and A. Ludwig. Adv. Funct. Mater. 20(2010). 1917
- [10] S. Seelecke and I. Müller, *Shape memory alloy actuators in smart structures: Modeling and simulation*, Appl. Mech. Rev. 57 (1) (2004), pp. 23–46. doi:10.1115/1.1584064
- [11] F. Wendler, H. Ossmer, C. Chluba, E. Quandt, and M. Kohl, *Mesoscale simulation of elastocaloric cooling in SMA films*, Acta Mater. 136 (2017) (2017), pp. 105–117. doi:10.1016/j.actamat.2017.06.044
- [12] C. Chluba, W. Ge, R.L. De Miranda, J. Strobel, L. Kienle, E. Quandt, and M. Wuttig, *Shape memory alloys. Ultralow-fatigue shape memory alloy films.*, Science 348 (2015), pp. 1004–1007. doi:10.1126/science.1261164
- [13] C. Chluba, H. Ossmer, C. Zamponi, M. Kohl, and E. Quandt, *Ultra-low fatigue quaternary TiNi-based films for elastocaloric cooling*, Shape Memory Superelasticity 2 (1) (2016), pp. 95–103. doi:10.1007/s40830-016-0054-3
- [14] E. Patoor, D.C. Lagoudas, P.B. Entchev, L.C. Brinson, and X. Gao, *Shape memory alloys, Part I: General properties and modeling of single crystals*, Mechanics Mater. 38 (2006), pp. 391–429. doi:10.1016/j.mechmat.2005.05.027
- [15] D.C. Lagoudas, P.B. Entchev, P. Popov, E. Patoor, L.C. Brinson, and X. Gao, *Shape memory alloys, Part II: Modeling of polycrystals*, Mechanics Mater. 38 (2006), pp. 430–462. doi:10.1016/j.mechmat.2005.08.003
- [16] J.E. Massad and R.C. Smith, *A homogenized free energy model for hysteresis in thin-film shape memory alloys*, Thin Solid Films 489 (1–2) (2005), pp. 266–290. doi:10.1016/j.tsf.2005.04.079
- [17] A. Coda, M. Urbano, L. Fumagalli, and F. Butera, *Investigation on the hysteretic behavior of NiTi shape memory wires actuated under quasi-equilibrium and dynamic conditions*, J. Mater. Eng. Perform. 18 (2009), pp. 725–728. doi:10.1007/s11665-009-9492-9
- [18] H. Ossmer, C. Chluba, M. Gueltig, E. Quandt, and M. Kohl, *Local evolution of the elastocaloric effect in TiNi-based films*, Shape Memory Superelasticity 1 (2) (2015), pp. 142–152. doi:10.1007/s40830-015-0014-3

- [19] H. Ossmer, C. Chluba, S. Kauffmann-Weiss, E. Quandt, and M. Kohl, *TiNi-based films for elastocaloric microcooling—Fatigue life and device performance*, *APL Mater.* 4 (6) (2016), pp. 064102. doi:[10.1063/1.4948271](https://doi.org/10.1063/1.4948271)
- [20] Y.J. He and Q.P. Sun, *Rate-dependent damping capacity of NiTi shape memory alloy*, *Solid State Phenomena* 172-174 (2011), pp. 37–42. doi:[10.4028/www.scientific.net/SSP.172-174](https://doi.org/10.4028/www.scientific.net/SSP.172-174)
- [21] L.C. Brinson, *Stress-induced transformation behavior of a polycrystalline NiTi shape memory alloy: Micro and macromechanical investigations via in situ optical microscopy*, *J. Mech. Phys. Solids* 52 (7) (2004), pp. 1549–1571. doi:[10.1016/j.jmps.2004.01.001](https://doi.org/10.1016/j.jmps.2004.01.001)
- [22] H. Soul, A. Isalgue, A. Yawny, V. Torra, and F.C. Lovey, *pseudoelastic fatigue of NiTi wires: Frequency and size effects on damping capacity*, *Smart Mater. Struct.* 19 (8) (2010), pp. 085006. doi:[10.1088/0964-1726/19/8/085006](https://doi.org/10.1088/0964-1726/19/8/085006)